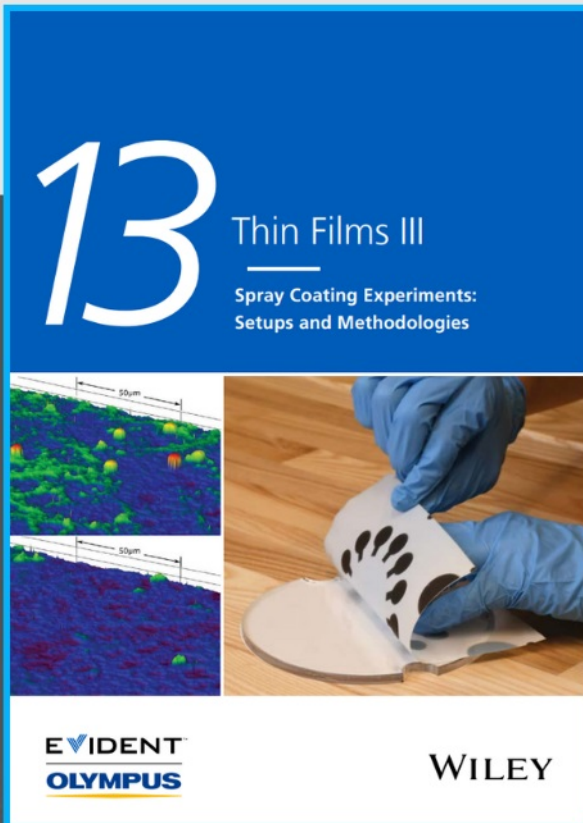




Spray Coating Experiments: Setups and Methodologies



**The latest eBook from
Advanced Optical Metrology.
Download for free.**

Spray Coating Experiments: Setups and Methodologies, is the third in our Thin Films eBook series. This publication provides an introduction to spray coating, three article digests from Wiley Online Library and the latest news about Evident's Image of the Year Award 2022.

Wiley in collaboration with Evident, are committed to bridging the gap between fundamental research and industrial applications in the field of optical metrology. We strive to do this by collecting and organizing existing information, making it more accessible and useful for researchers and practitioners alike.

EVIDENT
OLYMPUS

WILEY

Defect-Induced Atomic Arrangement in CoFe Bimetallic Heterostructures with Boosted Oxygen Evolution Activity

Lingxia Zheng, Weiqing Ye, Yijian Zhao, Zhuoqing Lv, Xiaowei Shi, Qi Wu,* Xiaosheng Fang,* and Huajun Zheng*

Three CoFe-bimetallic oxides with different compositions (termed as CoFeO_x-A/N/H) are prepared by thermally treating metal-organic-framework (MOF) precursors under different atmospheres (air, N₂, and NaBH₄/N₂), respectively. With the aid of vast oxygen vacancies (O_v), cobalt at tetrahedral sites (Co²⁺(Th)) in spinel Co₃O₄ is diffused into interstitial octahedral sites (Oh) to form rocksalt CoO and ternary oxide CoFe₂O₄ has been induced to give the unique defective CoO/CoFe₂O₄ heterostructure. The resultant CoFeO_x-H exhibits superb electrocatalytic activity toward water oxidation: overpotential at 10 mA cm⁻² is 192 mV, which is 122 mV smaller than that of CoFeO_x-A. The smaller Tafel slope (42.53 mV dec⁻¹) and higher turnover frequency (785.5 h⁻¹) suggest fast reaction kinetics. X-ray absorption spectroscopy, ex situ characterizations, and theoretical calculations reveal that defect engineering effectively tunes the electronic configuration to a more active state, resulting in the greatly decreased binding energy of oxo intermediates, and consequently much lower catalytic overpotential. Moreover, the construction of hetero-interface in CoFeO_x-H can provide rich active sites and promote efficient electron transfer. This work may shed light on a comprehensive understanding of the modulation of electron configuration of bimetallic oxides and inspire the smart design of high-performance electrocatalysts.

1. Introduction

Electrocatalytic water splitting is regarded as one of the most promising hydrogen production routes which is a renewable, clean, and environmentally benign source of energy.^[1–3] However, considerable energy consumption is required to drive the critical half-reaction, the kinetically sluggish oxygen evolution reaction (OER) at the anode, which is a complex stepwise four-electron redox process to enable the formation of oxygen-oxygen bonds.^[4–6] Presently, the state-of-the-art catalysts for OER are precious metal oxides (RuO₂ and IrO₂), while their limited resources and high expense seriously restrict the large-scale application. Thus, it is imperative to develop more efficient and earth-abundant catalysts to overcome the kinetic barrier and reduce the overpotential for OER.


3d transition metal oxides (TMOs) have recently been considered as promising alternatives owing to their merits of low-cost, abundant availability, and eco-friendly.^[7–10] As a variety of typical TMOs, spinel oxides (AB₂O₄) composed of two types of geometrical sites: metal ions A²⁺ in the center of tetrahedral sites (T_d) and metal ions B³⁺ bond in the center of octahedral sites (O_h), are of great interest as OER electrocatalysts given the virtue of exceptional activity, low-cost and robust stability in the alkaline media.^[11,12] Nevertheless, the electrochemical performance of spinel oxides is still unsatisfactory due to the limited number of reactive sites and inferior electrical conductivity. Therefore, numerous strategies have been exploited to improve the OER activity of TMOs. In particular, subtle engineering of the electron configuration of e_g orbitals in spinel oxides is an effective route as it determines the interaction strength with oxo intermediates toward OER, thereby facilitating the reaction kinetics.^[13,14] Sun et. al.^[15] reported that highly active Ni³⁺ (t_{2g}⁶e_g¹) species induced by oxidation in NiO@NiCo₂O₄ heterostructure were responsible for the enhanced OER. Tian et. al.^[16] revealed that both Ni³⁺ (t_{2g}⁶e_g¹) and Jahn–Teller active Mn³⁺ (t_{2g}³e_g¹) species enabled the promotion of O–O bond formation and thereby leading to excellent OER activity. Zhang et. al.^[17] suitably engineered the low-coordination atoms in NiO/Co₃O₄ heterointerfaces and achieved boosting electrocatalysts. Liu et. al.^[18] induced in-plane CoO@Co₃O₄ rocksalt@spinel heterophase, which delivered drastically improved OER activity. These achievements verify that the electrochemical ability of

L. Zheng, W. Ye, Y. Zhao, Z. Lv, X. Shi, H. Zheng
Department of Applied Chemistry
Zhejiang University of Technology
Hangzhou 310014, P. R. China
E-mail: zhenghj@zjut.edu.cn

L. Zheng, X. Shi, H. Zheng
Petroleum and Chemical Industry Key Laboratory of Organic
Electrochemical Synthesis
State Key Laboratory Breeding Base of Green Chemistry Synthesis
Technology
Zhejiang University of Technology
Hangzhou 310014, P. R. China

Q. Wu
School of Science and Institute of Oxygen Supply and Everest
Research Institute
Tibet University
Lhasa 850000, P. R. China
E-mail: wuqi@utibet.edu.cn

X. Fang
State Key Laboratory of Molecular Engineering of Polymers
Department of Materials Science
Fudan University
Shanghai 200433, P. R. China
E-mail: xshfang@fudan.edu.cn

 The ORCID identification number(s) for the author(s) of this article can be found under <https://doi.org/10.1002/smll.202205092>.

DOI: 10.1002/smll.202205092

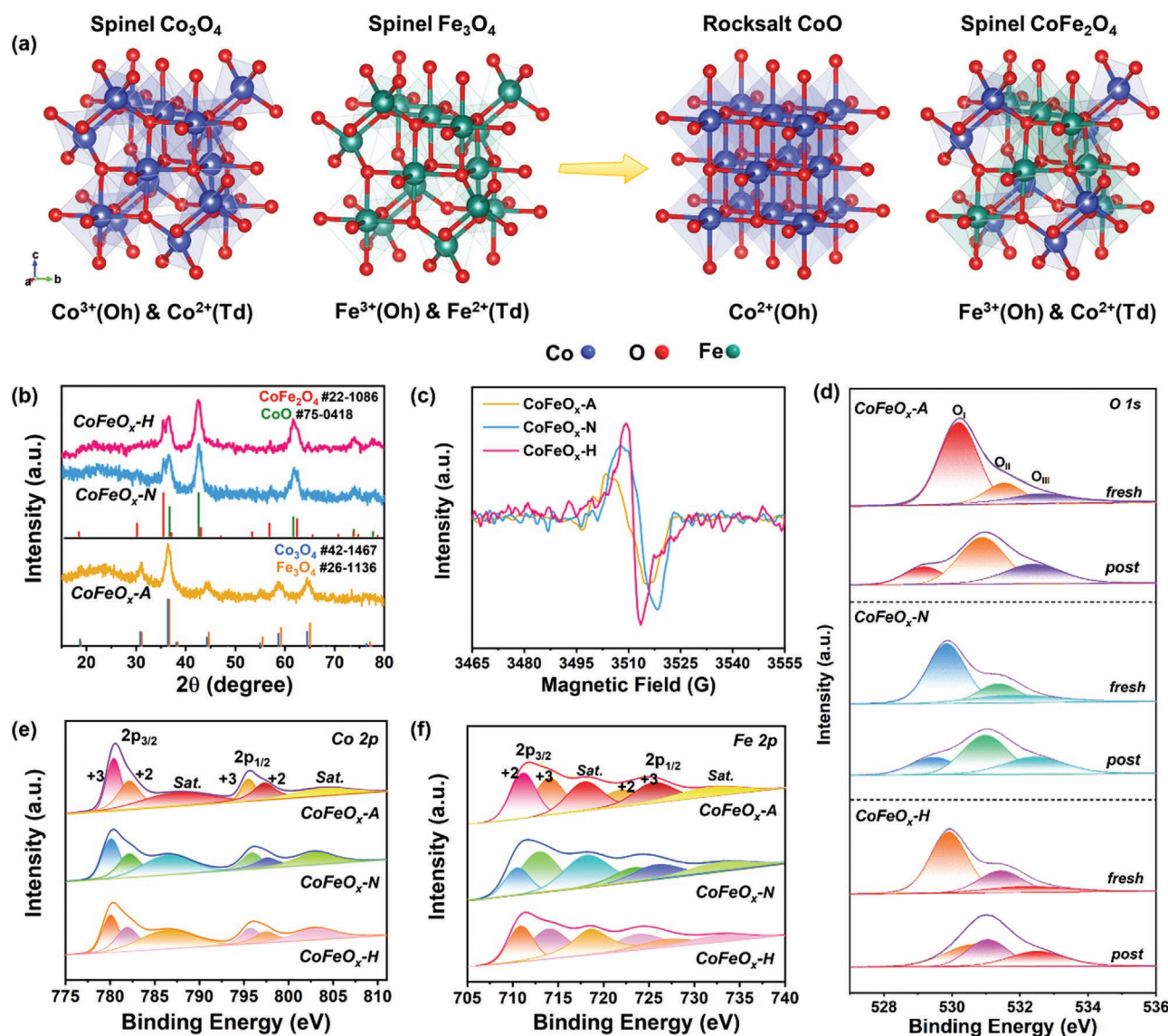


Figure 1. a) The geometrical configuration of spinel Co₃O₄, Fe₃O₄, CoFe₂O₄, and rocksalt CoO. b) X-ray diffraction (XRD) patterns and c) electron paramagnetic resonance (EPR) results of CoFeO_x-A/N/H. High-resolution X-ray photoelectron spectra (XPS) spectra of d) O 1s, e) Co 2p, f) Fe 2p.

3d TMOs could be much higher by tuning the electronic structure to a more active state given the powerful covalence of M-O bonds.^[19] Moreover, the construction of hetero-interface by taking full advantage of both two components is another effective means to enhance the electrocatalytic activity, which will promote electron transfer at the interface with a rapid reaction rate and offer abundant active sites.^[20–23]

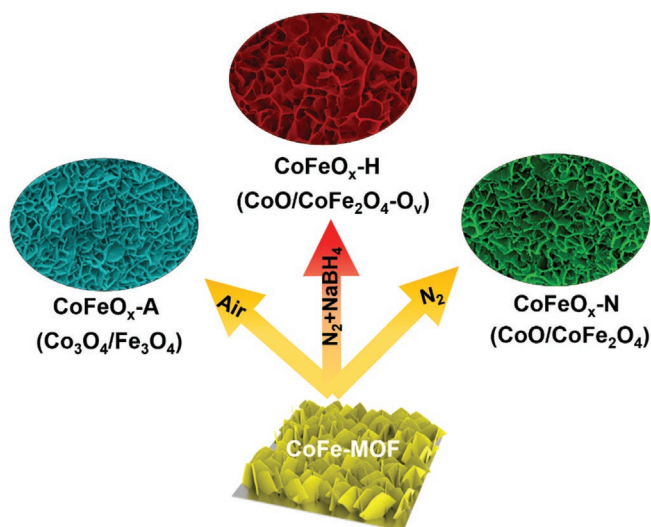
To date, proper incorporation of oxygen vacancies (O_v) in electrocatalysts is reported to result in higher catalytic activity and improved electronic conductivity.^[24–26] Regarding all the above advantages, herein, structural distinction CoO/CoFe₂O₄-O_v (CoFeO_x-H) heterostructure is constructed by the incorporation of abundant oxygen vacancies. Cobalt at tetrahedral sites (Co²⁺(Th)) in spinel Co₃O₄ is diffused into interstitial octahedral sites (Oh) to form rocksalt CoO and ternary oxide CoFe₂O₄ has been induced to give the unique defective CoO/CoFe₂O₄ heterostructures (Figure 1a). The numerous Co²⁺ (t_{2g}⁶e_g¹) active sites

and rich O_v are accounted for the superb electrocatalytic OER activity. The extended X-ray absorption fine structure (EXAFS) spectroscopy reveals the improvement of disordered degree at the hetero-interface and the enhancement of oxygen vacancy levels in the catalyst. Furthermore, density functional theory (DFT) calculations verify that the unique hetero-interface promotes the much smaller ΔG_{•O₂} based on the lower-lying d-band center and higher carrier concentration across the Fermi level of CoFeO_x-H.

2. Results and Discussion

2.1. Study of Structure and Morphology

Three different bimetallic oxides CoFeO_x are facily generated upon thermal treatment of MOF precursors in varied



Scheme 1. The preparation routes for the three bimetallic oxide composites CoFeO_x-A/N/H and the corresponding scanning electron microscopy (SEM) images.

atmospheres as illustrated in **Scheme 1**. X-ray diffraction (XRD) patterns were examined to reveal the crystal structures. The sharp characteristic peak at $\approx 10.5^\circ$ matches well with (112) plane of 2-methylimidazole^[27] for CoFe-MOF (Figure S1, Supporting Information), manifesting the successful synthesis of MOF precursor. Absolutely different compositions and electronic structures are obtained after different thermal treatments as displayed in Figure 1 for the three bimetallic oxides. A coexistence of spinel Co₃O₄ (JCPDS no. 42–1467) and spinel Fe₃O₄ (JCPDS no. 26–1136) is found in sample CoFeO_x-A (Figure 1b). Notably, the diffraction peaks in CoFeO_x-N and CoFeO_x-H can be assigned to rocksalt CoO (JCPDS no. 75–0418) and spinel CoFe₂O₄ (JCPDS no. 22–1086). Peaks at 36.7, 42.6, 61.8, 74.1, and 78.0° are ascribed to (111), (200), (220), (311) and (222) planes of CoO, while peaks at 35.4, 56.9, and 62.6° are assigned to (311), (511) and (440) crystalline planes of CoFe₂O₄. Impressively, the FWHM (full width at half maximum) of diffraction peaks in CoFeO_x-H are larger than those of CoFeO_x-N (Figure S2, Supporting Information),^[28] which implies smaller grain size based on Scherrer formula, manifesting that the reduction in NaBH₄ exerts a pronounce effect on the crystal structure. The result clearly demonstrates the geometrical transformation from spinel Co₃O₄/Fe₃O₄ to CoO/CoFe₂O₄ with the aid of vast oxygen vacancies (Figure 1a). To further reveal the difference between CoFeO_x-H and CoFeO_x-N, an inductively coupled plasma optical emission spectrometer (ICP-OES) was performed to determine the exact metal contents (Table S1, Supporting Information). Specifically, CoFeO_x-N contains 51.61% of Co and 29.06% of Fe, while CoFeO_x-H has 57.08% of Co and 24.98% of Fe. It suggests that different contents of Co and Fe exist in the two materials although they have very similar XRD profiles. Noteworthy, the total content of Co and Fe is almost the same for the two catalysts, and is higher than CoFeO_x-A, manifesting the loss of lattice oxygen and exposure of metal sites upon reduction treatment.

6 Electron paramagnetic resonance spectroscopy (EPR) was conducted to probe the evolution of oxygen defects. As shown

in Figure 1c, abundant oxygen vacancies can be found in the three catalysts with a *g* value of ≈ 2.00 , and CoFeO_x-H shows the strongest EPR signal compared to the counterparts. The increase of oxygen defects would result in the reduction of coordination numbers of adjacent metal atoms and the optimization of catalytic reactions.^[17] The negligible deviation in the *g* value may be due to a change in the spin state of the electrons.^[29] In addition, the core-level O 1s XPS spectra of CoFeO_x-A/N/H (Figure 1d) can be deconvoluted into three peaks in which O_I is related to metal-oxygen bonds (529.8 eV), O_{II} belongs to defect sites with low oxygen coordination (531.7 eV), and O_{III} represents surface OH⁻ groups at 532.3 eV.^[30] The much stronger intensity of peak O_{II} (25.74%) in CoFeO_x-H indicates a larger amount of oxygen vacancies compared with that of CoFeO_x-A (18.28%) and CoFeO_x-N (20.40%), in accordance with the EPR results. Thus, CoO/CoFe₂O₄ heterostructure with oxygen vacancies (CoO/CoFe₂O₄-O_v) was simulated for CoFeO_x-H to make distinguish from CoFeO_x-N, which will be discussed later. The overall XPS survey spectra (Figure S3, Supporting Information) display similar outlines for the three catalysts, revealing the presence of C, O, Fe and Co. The content of N element is $\approx 0.50\%$, 0.61 and 0.47% for CoFeO_x-A/N/H, respectively, which is possibly originated from the 2-methylimidazole (2-MI) ligand. Such a low content can be negligible and is hardly observed in the survey scan spectra. The Co 2p spectra of CoFeO_x-A/N/H (Figure 1e) show the representative spin-orbit splitting indications of *p* orbital along with two satellite peaks between 2p_{1/2} and 2p_{3/2}, suggesting the presence of Co²⁺ and Co³⁺ oxidation states.^[31] For CoFeO_x-H, binding energies (BEs) at 780.1 and 795.7 eV are assigned to Co³⁺, while 782.0 and 797.6 eV can be ascribed to Co²⁺. Similar spectral profiles are readily observed in the Fe 2p spectra of CoFeO_x-A/N/H (Figure 1f). BEs at 713.0 and 724.4 eV of CoFeO_x-H belong to Fe 2p_{3/2} and Fe 2p_{1/2} respectively, accompanied by two satellite peaks (717.8 and 732.2 eV).^[32] The high ratios of Co²⁺/Co³⁺ and Fe²⁺/Fe³⁺ (>1, Table S2, Supporting Information) in CoFeO_x-H are reported to be an indicator of more amount of oxygen defects.^[33–35] The results demonstrate that reasonable control of oxygen defects can be readily achieved by changing calcination conditions, which help regulate the surface electronic structure and charge distribution, thereby boosting the OER activity.

X-ray absorption spectroscopy (XAS) was probed into CoFeO_x-N and CoFeO_x-H catalysts to get more insight into the atomic structural distinctions between them. As shown in **Figure 2a**, the X-ray absorption near-edge structure (XANES) spectra of Co K-edge in both catalysts share similar profiles and are very close to that of CoO, in which there is a pre-edge at 7710.1 eV and a strong white line peak at 7726.6 eV, clearly demonstrating a dominant contribution of Co²⁺ in octahedral coordination. The pre-edge shifts slightly toward a lower energy direction (inset in Figure 2a), which suggests a lower average oxidation state of Co in CoFeO_x-H.^[35,36] The pre-edge of Fe K-edge XANES (Figure 2b) for both CoFeO_x-N and CoFeO_x-H is very close to that of FeO, and a relatively lower oxidation state of Fe is found in CoFeO_x-H compared to CoFeO_x-N. The lower oxidation states of bimetals in CoFeO_x-H indicate a higher level of vacancies. The Fourier transform of the EXAFS is employed to disclose the atomic configuration and the fitting data are summarized in Figures S4–S6, Tables S3 and S4 (Supporting Information).

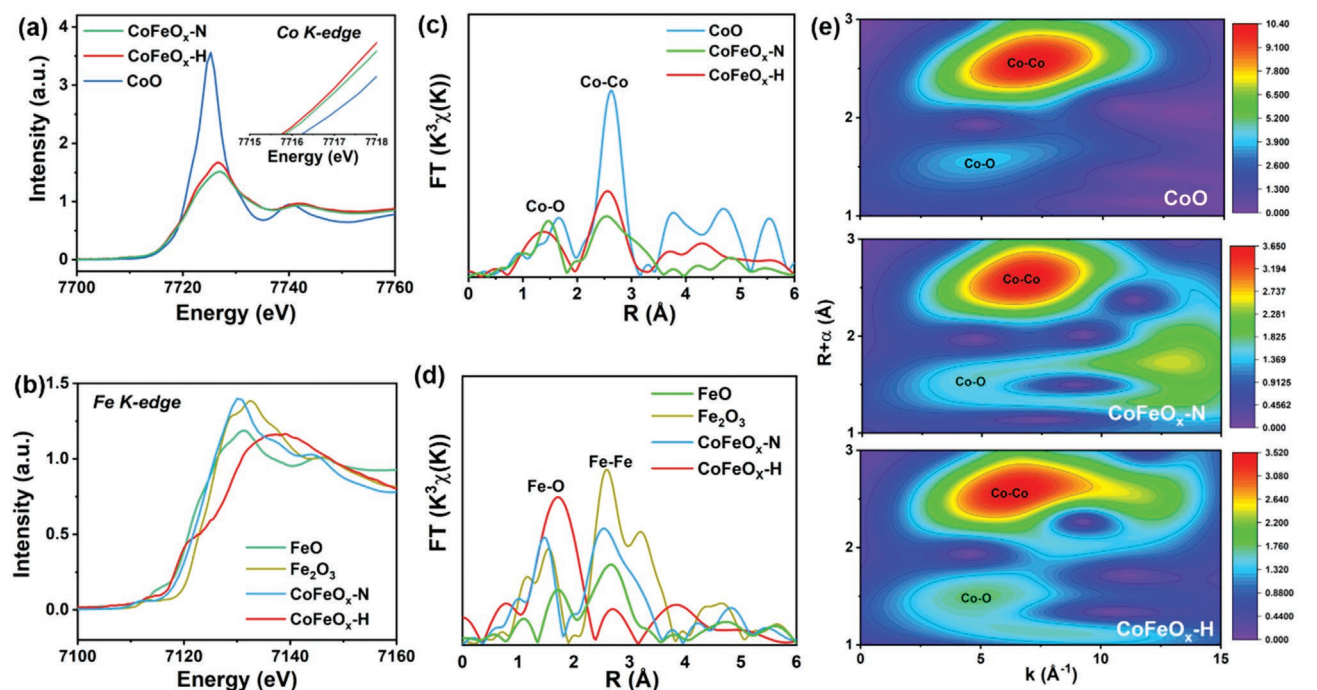


Figure 2. X-ray absorption near-edge structure (XANES) spectra of a) Co K-edge and b) Fe K-edge. Extended X-ray absorption fine structure (EXAFS) spectra of c) Co K-edge and d) Fe K-edge in R -space. e) Wavelet transforms for the k^3 -weighted EXAFS signals of Co k-edge in CoFeO_x-N and CoFeO_x-H with CoO as reference.

In the Co R -space spectra (Figure 2c), both CoFeO_x-N and CoFeO_x-H exhibit a peak ranging from 1–2 Å representing the Co-O shell.^[18] The cobalt cations at Oh sites have two different interatomic distances to neighboring metal ions at Oh sites (2.5 Å) and Td sites (3.1 Å) for CoFeO_x-N. While only a single peak centered at 2.5 Å can be found in CoFeO_x-H, suggesting that it is more close to the atomic structure of the CoO reference.^[37] The results verify that numerous Co²⁺ cations at Oh sites are produced in CoFeO_x-H and the electronic environment is accordingly arranged to result in the formation of CoO/CoFe₂O₄ heterostructure with O_v. The better electronic configuration of Co²⁺ ($t_{2g}^6e_g^1$) compared to that of Co³⁺ ($t_{2g}^6e_g^0$) is beneficial for OER activity.^[19] And the decreased distance of Co-O in CoFeO_x-H reveals an enhancement of the disorder degree. Evidently, the decreased coordination numbers of Co-Co in CoFeO_x-N and CoFeO_x-H (Table S3, Supporting Information) also suggest the increased disordered degree and high level of oxygen vacancies in catalysts.^[17] Similarly, Fe-O shell and the Fe cations at Oh sites can be found in the Fe K-edge EXAFS spectra for both CoFeO_x-N and CoFeO_x-H (Figure 2d), which is similar to that of the FeO reference. The evidently weaker Fe-Fe shell (2.6 Å) is attributed to the increase of disorder and decrease of Fe atom coordination numbers.^[38–40] Accordingly, an intensity maximum at $\approx 6.5 \text{ \AA}^{-1}$ correlated with the Co-Co/Fe path in CoFeO_x-N and CoFeO_x-H is observed as verified by the wavelet transform results in Figure 2e, suggesting the lower coordination configuration of Co, consistent with the EXAFS results.^[17]

Morphological structures of CoFe-MOF (Figure S7, Supporting Information) and CoFeO_x-A/N/H (Figure 3) were examined by scanning electron microscopy (SEM) analysis.

All of them exhibit a conventional hierarchical 2D-nanosheet array morphology in which the nanosheets are standing vertically on the surface of Ni foamed substrate to form a porous network with large uniform distribution, which suggests that the microstructures are well retained after thermal treatment in any atmosphere. Noteworthy, in contrast to the smooth and ultrathin sheets in CoFe-MOF, the thick and rough surface of the nanosheets along with many tiny nanoparticles residing at the edges of the sheets are observed in CoFeO_x-A (Figure 3a–c) and CoFeO_x-N (Figure 3d–f). While CoFeO_x-H bears a porous and clean surface of the nanosheets (Figure 3g–i) featuring an ultrathin layer (thickness of 3–4 nm from the atomic force microscope (AFM) results in Figure S8, Supporting Information). The length of the three nanoarray films is almost the same ($\approx 0.50 \mu\text{m}$, Figure 3c,f,i).

Transmission electron microscope (TEM) results provide more insight into the morphological features of CoFeO_x-A/N/H. The corrugated sheet-like morphology with good transparency verifies the ultrathin mesoporous network (Figure 4a–c), consistent with the SEM observation. The dark strips suggest the wrinkles or foldable edges of the nanosheets. In contrast to catalyst CoFeO_x-A (Figure 4a) and CoFeO_x-N (Figure 4b), much more randomly oriented crystallites are presented on the few-layered nanosheets in CoFeO_x-H (Figure 4c). It is noteworthy that the unique structural features of all three samples enable abundant active sites exposed to the electrolyte and facilitated ion transport. Evidentially, the specific surface area value determined by Brunauer-Emmett-Teller (BET) (Figure S9, Supporting Information) is calculated to be $110.44 \text{ m}^2 \text{ g}^{-1}$ for CoFeO_x-H, significantly greater than that of CoFeO_x-A ($74.03 \text{ m}^2 \text{ g}^{-1}$) and CoFeO_x-N ($82.14 \text{ m}^2 \text{ g}^{-1}$).

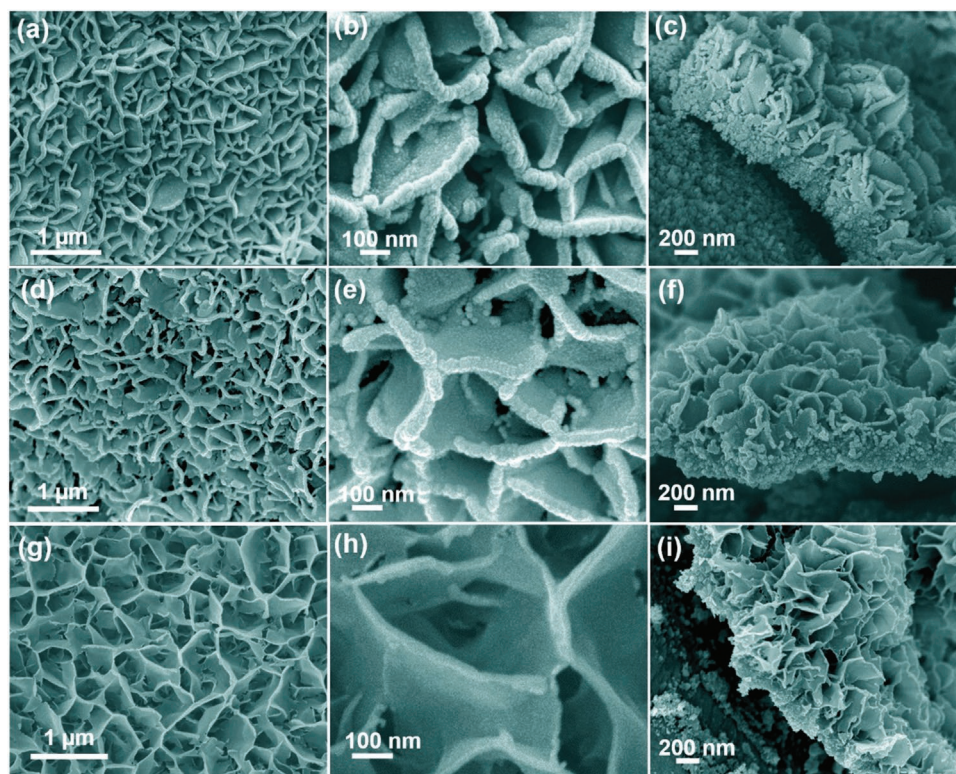


Figure 3. Scanning electron microscopy (SEM) images of a–c) $\text{CoFeO}_x\text{-A}$, d–f) $\text{CoFeO}_x\text{-N}$, and g–i) $\text{CoFeO}_x\text{-H}$.

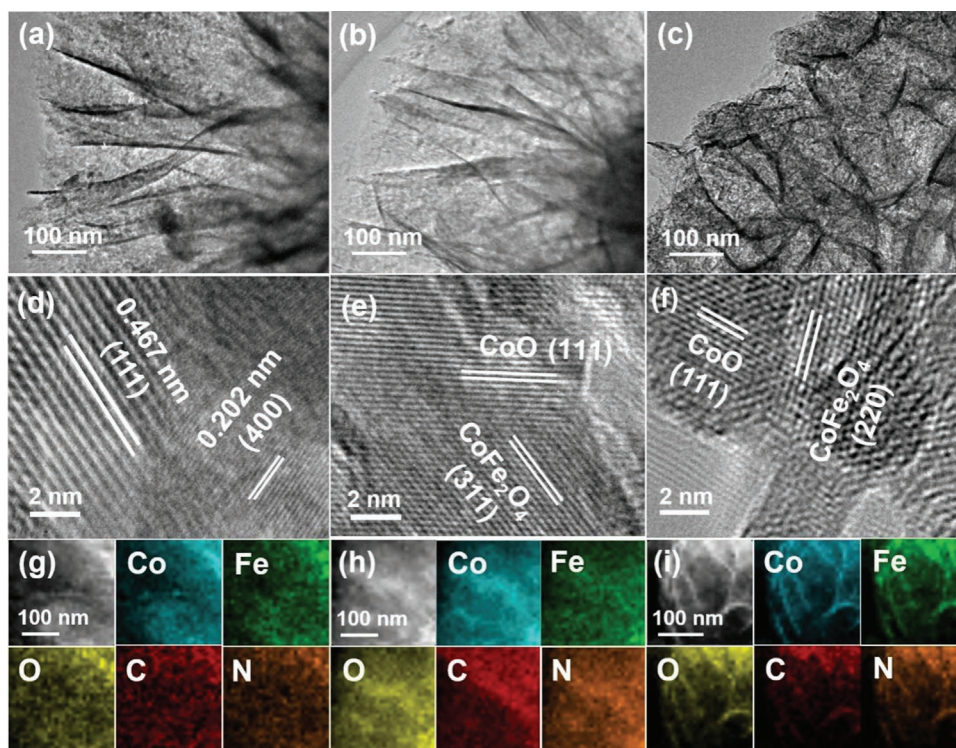


Figure 4. a–c) Transmission electron microscopy (TEM) images, d–f) high resolution (HR)-TEM images, and g–i) TEM-EDS (energy dispersive X-ray spectroscopy) mapping of $\text{CoFeO}_x\text{-A}$, $\text{CoFeO}_x\text{-N}$, and $\text{CoFeO}_x\text{-H}$, respectively.

The isotherms for all show typical IV hysteresis loops around the relative pressure of 1.0, implying the mesoporous feature. Both $\text{CoFeO}_x\text{-A}$ and $\text{CoFeO}_x\text{-N}$ exhibit a small peak centered at ≈ 2.4 nm, while a distinct peak at ≈ 5.00 nm is observed for $\text{CoFeO}_x\text{-H}$. In this regard, $\text{CoFeO}_x\text{-H}$ endows abundant electroactive sites and desired mesoporous structure, which would facilitate the access of electrolytes and fast mass transfer for OER reactions.^[41–43] The high resolution (HR)-TEM results are in accordance with the XRD patterns (Figure 1b). The lattice fringes of $\text{CoFeO}_x\text{-A}$ with interplanar spacings of 0.202 and 0.467 nm can be assigned to the (400) and (111) planes of Co_3O_4 and Fe_3O_4 (Figure 4d), respectively. For $\text{CoFeO}_x\text{-N}$, the lattice fringe of CoFe_2O_4 is 0.253 nm, corresponding to the (311) facet, while CoO presents the (111) plane with a spacing of 0.245 nm (Figure 4e). The observed lattice spacings of $\text{CoFeO}_x\text{-H}$ (Figure 4f) are 0.246 nm and 0.296 nm, assigned to the (111)

planes of CoO and (220) plane of CoFe_2O_4 , respectively. In addition, the EDS mapping results in Figure 4g–i show the uniform dispersion of the elements Co, Fe, O, C, and N throughout the nanosheets. The C and N are derived from the organic ligands of 2-MI.

2.2. Evaluation of Electrocatalytic Performance

The electrocatalytic performance of $\text{CoFeO}_x\text{-A/N/H}$ was evaluated in 1.0 mol L^{-1} KOH, and the main parameters are summarized in Table S5 (Supporting Information). The *i*R compensated polarization curves reveal that $\text{CoFeO}_x\text{-H}$ exhibits much enhanced OER activity compared with the other two samples, and all three catalysts endow better electrocatalytic behavior than RuO_2 (Figure 5a). The overpotential

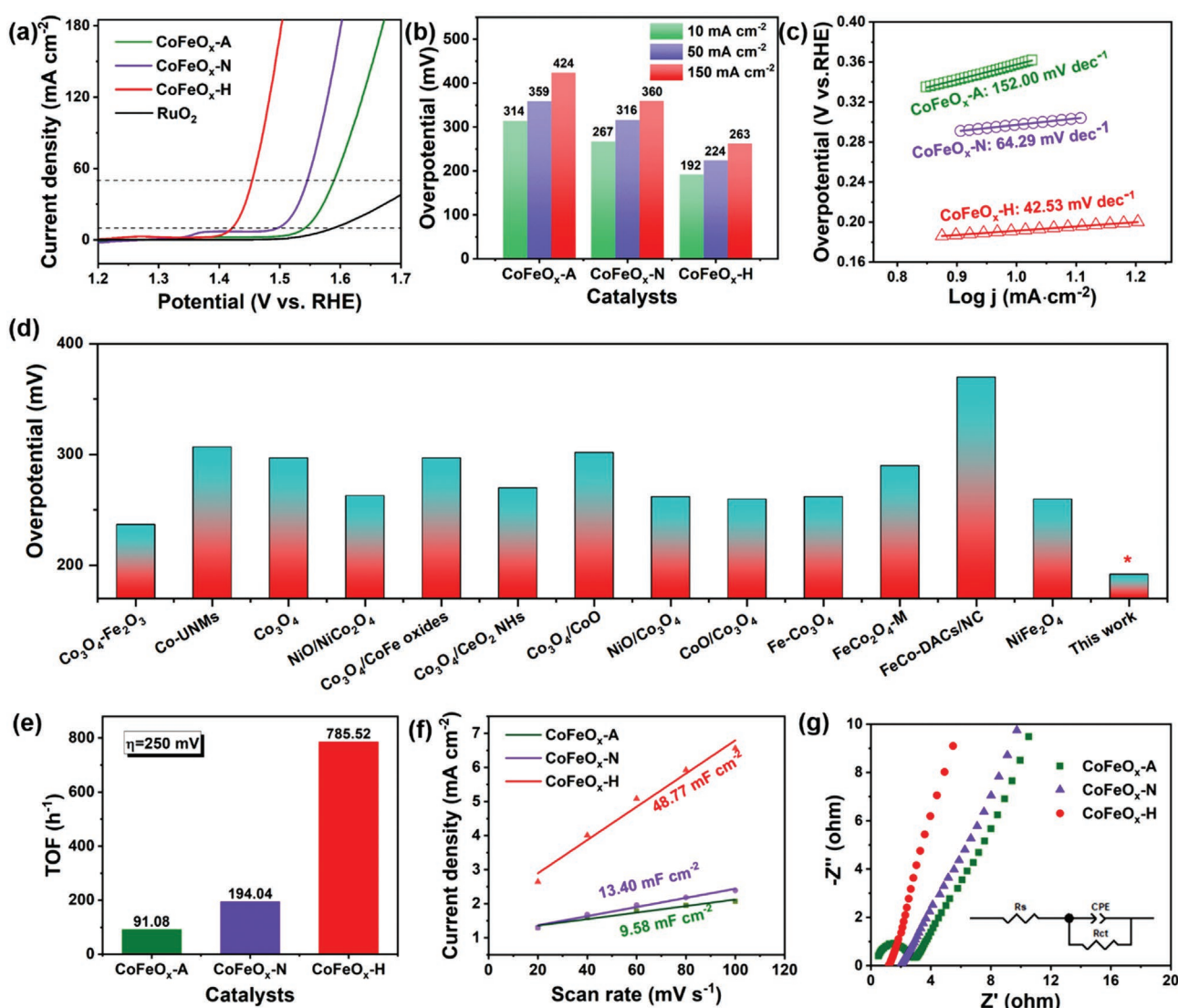


Figure 5. Electrochemical performance of $\text{CoFeO}_x\text{-A/N/H}$ catalysts. a) Compensated polarization curves at 5 mV s^{-1} . b) A comparison of overpotential values at 10, 50, and 150 mA cm^{-2} of the three catalysts. c) Tafel plots. d) Overpotential at 10 mA cm^{-2} of $\text{CoFeO}_x\text{-H}$ (referred as This work) and the related catalysts in literatures. e) The turnover frequency (TOF) of the three catalysts toward water oxidation. f) Capacitive current densities as a function of scan rates to evaluate the electrochemically active surface area (ECSA). g) Electrochemical impedance spectroscopy (EIS) results (inset: equivalent circuit).

at 10 mA cm⁻² is only 192 mV, which is much lower than that of CoFeO_x-A (314 mV), CoFeO_x-N (267 mV) and RuO₂ (360 mV). Impressively, CoFeO_x-H shows the lowest overpotential values at 50 (224 mV) and 150 mA cm⁻² (263 mV), indicating the prospect for industrial application (Figure 5b). Meanwhile, it exhibits the smallest Tafel slope (42.53 mV dec⁻¹) compared with that of CoFeO_x-N (64.29 mV dec⁻¹) and CoFeO_x-A (152.00 mV dec⁻¹) as shown in Figure 5c, suggesting the fastest OER kinetics toward water oxidation. The delivered OER performance is better than most cobalt-based catalysts reported recently in literatures tested under the same condition (1 M KOH electrolyte) (Figure 5d and Table S6, Supporting Information). Moreover, the turnover frequency (TOF) of CoFeO_x-H is determined to be 785.5 h⁻¹ (at η = 250 mV), which is almost 9-fold larger than that of the CoFeO_x-A and four times larger than that of CoFeO_x-N, faithfully verifying the splendid intrinsic OER activity (Figure 5e). The faradaic efficiency (FE) was determined by using a rotating ring-disk electrode (RRDE) (Figures S10 and S11, Supporting Information) and the calculated values are 94.56%, 95.55%, and 99.15% for CoFeO_x-A/N/H, respectively, at 1.525 V versus RHE, which manifests that the water oxidation reaction is dominant compared with the electrochemical oxidation of metal sites.^[44–46]

The long-term durability of three catalysts CoFeO_x-A/N/H was assessed by conducting the chronoamperometry (CA) measurements at a constant overpotential. As shown in Figure S12a (Supporting Information), negligible variation of current density can be observed for CoFeO_x-A/N/H after a 24-h continuous electrocatalytic reaction, suggesting that all of them possess splendid long-term stability. This observation is consistent with the polarization results and EIS spectra before and after the durability test (Figures S13–15, Supporting Information) for CoFeO_x-A/N/H, respectively. While the commercial RuO₂ catalyst on nickel foam shows moderate stability with 93.3% retention after the 24h-OER test (Figure S12b, Supporting Information). It is safe to conclude that all three catalysts endow outstanding durability, and are promisingly applicable in practice. The Fe content in the solution after the 24 h OER test is lower than 0.001 mg (Table S7, Supporting Information), suggesting that the little loss of Fe species may not have a notable effect on the OER activity.^[47,48] As a reference, the post-OER catalysts CoFeO_x-A/N/H were further characterized by SEM (Figure S16, Supporting Information). It can be seen that the hierarchical nanosheet array structures of all three catalysts are well maintained without collapse, which evidently proves the robustness and long-term stability. BEs of Co 2p and Fe 2p of post CoFeO_x-N and CoFeO_x-H (Figure S17, Supporting Information) shift to lower binding energy after durability tests, suggesting the prominent change of electronic structure. Impressively, the significantly decreased ratio of Co²⁺/Co³⁺ (Table S2, Supporting Information) implies that numerous Co²⁺ have been oxidized to active Co³⁺ in the post CoFeO_x-H.^[49] The decreased O_I peak and increased O_{III} peak suggest the formation of Co/Fe (oxy)hydroxides on the surface after long-term durability (Figure 1d). While the markedly increased peak intensity of O_{II} in the post three catalysts implies the great stability of oxygen vacancies.^[50–52]

2.3. Origin study of the Superb OER Activity

To get more insight into the intrinsic OER catalytic activity, electrochemically active surface area (ECSA) was calculated based on the measured double-layer capacitance (C_{dl}) at varied scan rates from 20 to 100 mV s⁻¹ (Figure S18, Supporting Information) using the following equation: ECSA = C_{dl}/C_s, where C_s refers to the surface bilayer capacitance of the ideal smooth electrode (40 μF cm⁻²).^[53,54] As displayed in Figure 5f, CoFeO_x-H exhibits the highest C_{dl} (48.77 mF cm⁻²), and the calculated ECSA is ≈1219 cm² (inset in Figure S19, Supporting Information), which is 3.6 times greater than that of CoFeO_x-N (335 cm²) and 5.1 times greater than that of CoFeO_x-A (240 cm²). The vast ECSA can be possibly ascribed to the corrugated silky-like features of nanosheets allowing exposure of numerous active sites, which contributes remarkably to the boosted OER activity. Impressively, the ECSA-normalized polarization curves (Figure S19, Supporting Information) also reveal the outstanding intrinsic activity of CoFeO_x-H toward OER. To unveil the electron transfer kinetics, EIS tests were performed (Figure 5g) and the resistance values are fitted based on the equivalent circuit in the inset. CoFeO_x-H endows dramatically smaller intrinsic resistance (R_s, 1.24Ω) and charge transfer resistance (R_{ct}, 8.45 Ω) than that of CoFeO_x-A (2.74 and 16.91 Ω) and CoFeO_x-N (2.01 and 18.47 Ω) (Table S5, Supporting Information), validating favorable faradaic process and fast charge-transfer kinetics, and thereby promoting outstanding electrocatalytic OER activity.

DFT computation was employed to further disclose the origin of the superior electrocatalytic performance for OER. Based on the experimental results (XRD HRTEM and XAS), three heterostructures Co₃O₄/Fe₃O₄ (CoFeO_x-A) and CoO/CoFe₂O₄ (CoFeO_x-N) and CoO/CoFe₂O₄-O_v (CoFeO_x-H) are constructed and the optimized configurations are shown in Figure 6a–c, respectively. The possible position of O_v in CoFeO_x-H has been examined and the vacancy formation free energy (E_{Ov}) is calculated based on the following equation: E_{Ov} = E_v - E_p + μ_O, where E_v and E_p are the total energies of the defective and perfect CoO/CoFe₂O₄, respectively. μ_O is the chemical potential of the removed O atom. The O_{v1} at the interface of CoO/CoFe₂O₄ (Figure S20, Supporting Information, Figure 6c) endows the lowest vacancy formation energy (0.93 eV) and is chosen as the model structure. The free energy diagram toward OER on the surface of TMOs was calculated based on the computational hydrogen electrode model.^[55] The formation of gaseous O₂ includes four electrochemical steps (details in Supporting Information), where the elementary steps are a first-order of potential-dependent activity. The most positive energy difference of the three heterostructures occurs at the third step (Figure 6d), i.e., the formation of *OOH, which becomes the potential determining step (PDS). Specifically, the calculated energy changes of the PDS (G_{*OOH} - G_{*O}) for CoFeO_x-A, CoFeO_x-N, and CoFeO_x-H are 2.75 eV, 1.92 eV, and 1.45 eV, respectively (Figure 6e), implying that CoFeO_x-H possesses the best OER activity. The remarkable energy difference can be ascribed to the effective modulation of the electronic structure of adsorbed metal sites during OER. Differential charge density contour of CoFeO_x-N (Figure 6f) and CoFeO_x-H (Figure 6g) suggest that the charge density of active sites (dash circles) decreases after incorporation of vast O_v. The electron losses are found to be

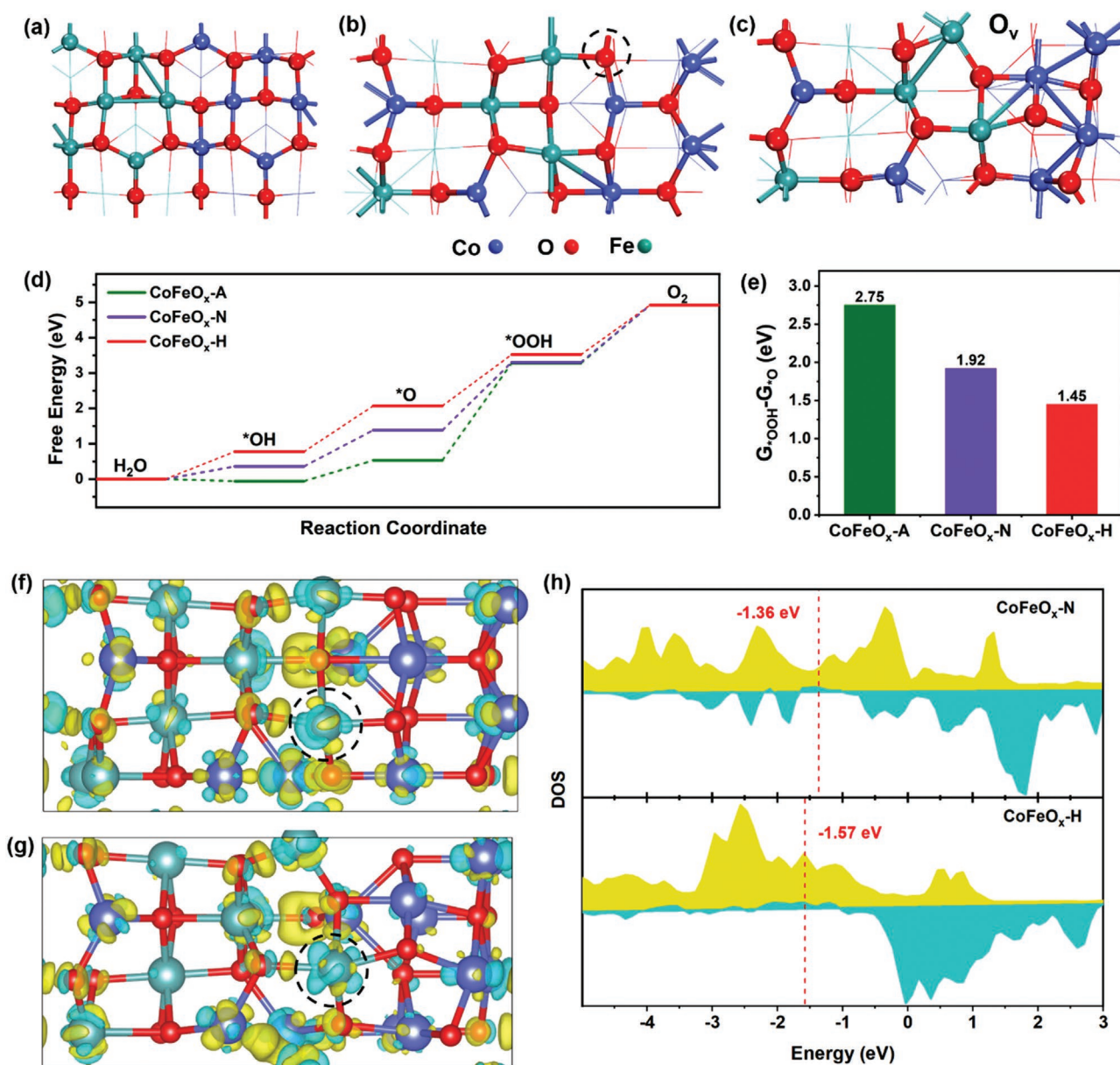


Figure 6. The model structures of a) CoFeO_x-A (Co₃O₄/Fe₃O₄), b) CoFeO_x-N (CoO/CoFe₂O₄), and c) CoFeO_x-H (CoO/CoFe₂O₄-O_v). d) Calculated free energy diagrams e) Gibbs free energy of the potential-determining step (ΔG_{*OOH}-ΔG_{*O}). Charge density difference diagrams of f) CoFeO_x-N and g) CoFeO_x-H. Iso-surface value is set to be 0.003 e Å⁻³. Yellow and cyan represent charge accumulation and depletion, respectively. h) Calculated total density of states (DOS) results of CoFeO_x-N and CoFeO_x-H. The dash lines represent the corresponding energy level of *d* band center of active metal sites and the Fermi level is set to 0 eV.

1.3013 and 1.3951, respectively, according to Bader charge analysis. The prominent electron loss of CoFeO_x-H indicates that the oxidation state of the surrounding Fe atom increases effectively and leads to higher OER activity. More interestingly, the number of electrons transferred to *O also increases compared to that of CoFeO_x-N, which is also beneficial for the reduction of the reaction energy barrier. The calculated *d*-band centers of the active sites on CoFeO_x-A and CoFeO_x-N and CoFeO_x-H are -1.16 eV (Figure S21, Supporting Information), -1.36 eV, and -1.57 eV (Figure 6h), respectively. According to the well-documented average *d*-band theory, the Fe atoms at the interface

with a lower *d*-band center may possess weaker and more suitable adsorption of oxygen intermediates, thereby resulting in relatively high OER activity. Therefore, the lower-lying *d*-band center and higher carrier concentration across the Fermi level of CoO/CoFe₂O₄-O_v correspond to a much smaller Gibbs energy barrier of the PDS, suggesting enhanced electrocatalytic activity toward OER. Furthermore, as is a general consensus that catalysts would undergo surface reconstruction and metal oxyhydroxides are the true active sites for OER. Structural models of FeCoOOH and FeCoOOH-O_v have been built (Figure S22, Supporting Information). FeCoOOH (001) surface is constructed by

doping a Fe atom on the surface of CoOOH (001), whose unit cell adopts a space group of P63/mmc with calculated lattice constants of $a = 2.88 \text{ \AA}$, $b = 2.88 \text{ \AA}$ and $c = 8.61 \text{ \AA}$. The lattice oxygen between Co and Fe is removed to construct the model of FeCoOOH- O_V in order to further elaborate the effect of oxygen vacancy on catalytic activity. As demonstrated in Figure S23, the Gibbs free energy barrier for the PDS of FeCoOOH- O_V is calculated to be 1.40 eV, much lower than that of FeCoOOH (1.58 eV). Accordingly, density of state (DOS) results (Figure S24, Supporting Information) reveal that FeCoOOH- O_V is more conducive to the electron transfer between the metal site and reaction intermediates. Collectively, both two kinds of structure models verify the modulated electronic structure and optimized Gibbs free energy barrier upon defect engineering, leading to enhanced electrocatalytic activity toward OER, which is in accordance with the experimental results.

3. Conclusions

In summary, a unique heterostructure electrocatalyst embracing vast oxygen vacancies (CoFeO_x-H) is designed by thermally annealing CoFe-MOF precursor in NaBH₄/N₂ atmosphere, which demonstrates more splendid electrocatalytic activity toward OER and fast reaction kinetics than the counterparts annealed in air (CoFeO_x-A) and nitrogen (CoFeO_x-N). The morphological and structural differences as well as the variation of the coordination environment have been thoroughly probed. DFT computations further reveal that the lower-lying *d*-band center and higher carrier concentration across the Fermi level lead to remarkably decreased Gibbs energy barrier of PDS, thus boosting OER activity. The work might shed light on a comprehensive understanding of the modulation of the electron configuration of bimetallic oxides and inspire the smart design of high-performance TMO catalysts.

4. Experimental Section

Synthesis of CoFe-MOF Precursors: The MOF precursors were prepared via a facile one-step solvothermal process. Typically, 2.24 mmol of Co(NO₃)₂·6H₂O and 0.16 mmol Fe(NO₃)₃·9H₂O were dissolved in 20 mL methanol, which was then added into 20 mL of 3 mmol 2-methylimidazole (2-MI, 0.262 g) methanol solution. The mixture was stirred magnetically to give a pinkish-purple homogeneous solution, and was then transferred to autoclave with cleaned Ni foam (NF) inside to undergo a solvothermal process by heating at 120 °C for 2 h. After reactions, CoFe-MOF precursor was obtained after washing and drying.

Synthesis of CoFeO_x-A/N/H: Three different atmospheres (air, N₂, and NaBH₄/N₂) were used to thermally treat CoFe-MOF precursors at 350 °C for 2 h to yield bimetallic oxides with different compositions. CoFeO_x-H was obtained by heating under a nitrogen stream with 0.5 g of NaBH₄ powder placed upstream in a tube furnace, while CoFeO_x-A and CoFeO_x-N were obtained by heating in air and under a nitrogen stream, respectively (Scheme 1). The mass loading of CoFeO_x-A/N/H was examined to be 0.425, 0.450, and 0.450 mg cm⁻², respectively.

Material Characterization: X-ray diffraction (XRD) was recorded on a BrukerAXS D8 Advance powder X-ray Cu K α radiation diffractometer from Germany (operating at 40 mA, 40 kV, $\lambda = 1.5405 \text{ \AA}$). Scanning electron microscope (SEM, ZEISS GeminiSEM, Germany) and High-resolution transmission electron microscope (HRTEM) equipped with

an energy dispersive X-ray spectroscopy (EDS, Tecnai G2 F30 TEM) were performed to study the morphologies. X-ray photoelectron spectra (XPS) were collected on a Thermo Scientific K-Alpha. The thickness of the nanosheet was measured with an atomic force microscope (AFM, Bruker Dimension Icon). An Inductively coupled plasma optical emission spectrometer (ICP-OES, Agilent 720ES) was performed to examine the metal content in the oxides. The porous features including specific surface area and pore size distribution were measured by Brunauer-Emmett-Teller (BET, MicroActive for ASAP 2460 Version, US) method. Electron paramagnetic resonance spectroscopy (EPR, Bruker EMXPLUS) was used to study the defect effects. The X-ray absorption spectroscopy (XAS) including X-ray absorption near-edge structure (XANES) and extended X-ray absorption fine structure (EXAFS) were obtained at the Beamline of TLS07A1 in National Synchrotron Radiation Research Center (NSRRC, Taiwan).

Electrochemical Measurements: Electrochemical tests were conducted on CHI 720D using a three-electrode system with 1.0 mol L⁻¹ KOH electrolyte. The sample on the Ni foam was used directly as the working electrode, Hg/HgO electrode and platinum sheet were used as the reference electrode and counter electrode respectively. To evaluate the electrocatalytic activity, RuO₂ electrode was tested under the same circumstance. Linear sweep voltammetry (LSV) with iR compensation was measured at a scanning rate of 5 mV s⁻¹. All the measured potentials were calibrated by reversible hydrogen electrode (RHE), and the formula is as follows: $E_{(RHE)} = E_{(Hg/HgO)} + 0.098 + 0.0591 \text{ pH}$. The overpotential (η) is obtained based on the formula: $\eta = E_{(RHE)} - 1.23$.

A rotating ring-disk electrode (RRDE) was used to measure the OER Faradaic efficiency (FE) of the three catalysts in 1 M KOH purged with N₂, and the collection efficiency (N) was determined by using a ferrocenyl redox probe method (Figure S10, Supporting Information).^[56–58] For the preparation of the catalyst on the disk electrode, 3 mg powdery catalyst was dispersed in 180 μL of ethanol and 20 μL 5 wt.% Nafion solution by sonication. Then 4 μL of the catalyst ink was drop-cast onto the glass carbon (GC) electrode with a loading of 0.48 mg cm⁻². The surface area of the disk electrode was 0.126 cm².

Computational Details: Vienna abinitio simulation package (VASP) was used to perform all the spin-polarized computations.^[59,60] The projector augmented wave method^[61] was used to describe the ion-electron interactions and Perdew-Burke-Ernzerhof (PBE) form was used to describe the general gradient approximation.^[62,63] The convergence criterion was fixed to be 0.03 eV \AA^{-1} and 10⁻⁵ eV for the residual force and energy, respectively, during structure relaxation. A supercell consisting of 1 \times 2 \times 1 Co₃O₄ (110) facet and 1 \times 2 \times 1 Fe₃O₄ (110) facet were used as the models for Co₃O₄ and Fe₃O₄, respectively. On this basis, two-third of Co atoms were replaced by Fe atoms to construct the model of CoFe₂O₄. The Co₃O₄/Fe₃O₄ (CoFeO_x-A) and CoO/CoFe₂O₄ (CoFeO_x-N) heterostructures were constructed according to a previous study.^[18] A surface O atom was removed from CoO/CoFe₂O₄ heterostructure to simulate the CoO/CoFe₂O₄ heterostructure with O vacancy (O_V), i.e., CoO/CoFe₂O₄- O_V (CoFeO_x-H). For the structure optimization, Brillouin zones were sampled by a Monkhorst-Pack 4 \times 3 \times 1 and 2 \times 6 \times 1 *k*-point grid for pristine structures and heterostructures, respectively. The *k*-point grid was doubled for the computation of density of states (DOS). The vacuum space over 15 \AA was employed in order to avoid the interaction between two periodic units. Bader charge analysis was carried out to account for the quantitative description of charge distribution and charge transfer. The free energy change (ΔG) of each elementary reaction was calculated based on the computational hydrogen electrode (CHE) model^[53]: $\Delta G = \Delta E + \Delta E_{ZPE} - T\Delta S$, where *T*, ΔS , ΔE , and E_{ZPE} is the temperature, entropy, reaction energy difference, zero-point energy, respectively.

Supporting Information

Supporting Information is available from the Wiley Online Library or from the author.

Acknowledgements

The authors would like to acknowledge the financial supports from Natural Science Foundation of Zhejiang Province (No. LY21B030005), the Key Project of Science and Technology of Zhejiang Province (No. 2020C03G2022586), and Natural Science Foundation of China (No. 51702287 and 21902143). [Correction added after publication 1 March 2023: Huajun Zheng and Qi Wu were reported as corresponding authors.]

Conflict of Interest

The authors declare no conflict of interest.

Data Availability Statement

The data that support the findings of this study are available in the supplementary material of this article.

Keywords

CoFe bimetallic oxides, defect engineering, electronic structure modulation, oxygen evolution reaction, spinel oxides

Received: August 19, 2022

Revised: December 1, 2022

Published online: December 19, 2022

- [1] C. G. Morales-Guio, L.-A. Stern, X. Hu, *Chem. Soc. Rev.* **2014**, *43*, 6555.
- [2] L. X. Zheng, F. Teng, X. Y. Ye, H. J. Zheng, X. S. Fang, *Adv. Energy Mater.* **2020**, *10*, 1902355.
- [3] L. Zheng, X. Ye, X. Deng, Y. Wang, Y. Zhao, X. Shi, H. Zheng, *ACS Sustainable Chem. Eng.* **2020**, *8*, 15906.
- [4] C. Huang, S. Cheng, L. Yu, W. Zhang, J. Zhou, Y. Zhang, Y. Yu, *Mater Today Phys* **2019**, *11*, 100162.
- [5] F. Yu, L. Yu, I. K. Mishra, Y. Yu, Z. F. Ren, H. Q. Zhou, *Mater Today Phys* **2018**, *7*, 121.
- [6] L. Zheng, S. Han, H. Liu, P. Yu, X. Fang, *Small* **2016**, *12*, 1527.
- [7] X.-Y. Yu, Y. Feng, B. Guan, X. W. (D.) Lou, U. Paik, *Energy Environ. Sci.* **2016**, *9*, 1246.
- [8] K. Xu, H. Ding, K. Jia, X. Lu, P. Chen, T. Zhou, H. Cheng, S. Liu, C. Wu, Y. Xie, *Angew. Chem., Int. Ed.* **2016**, *55*, 1710.
- [9] W. Liu, J. Xie, Y. Guo, S. Lou, L. Gao, B. Tang, *J. Mater. Chem. A* **2019**, *7*, 24437.
- [10] W. Sun, X. Tao, P. Du, Y. Wang, *Chem. Eng. J.* **2019**, *366*, 622.
- [11] M. Casas-Cabanas, G. Binotto, D. Larcher, A. Lecup, V. Giordani, J. M. Tarascon, *Chem. Mater.* **2009**, *21*, 1939.
- [12] H. Ding, H. Liu, W. Chu, C. Wu, Y. Xie, *Chem. Rev.* **2021**, *121*, 13174.
- [13] Y. Zhu, W. Zhou, Z.-G. Chen, Y. Chen, C. Su, M. O. Tade, Z. Shao, *Angew. Chem., Int. Ed.* **2015**, *54*, 3897.
- [14] S. Zhou, X. Miao, X. Zhao, C. Ma, Y. Qiu, Z. Hu, J. Zhao, L. Shi, J. Zeng, *Nat. Commun.* **2016**, *7*, 11510.
- [15] S. Sun, X. Jin, B. Cong, X. Zhou, W. Hong, G. Chen, *J. Catal.* **2019**, *379*, 1.
- [16] T. Tian, H. Gao, X. Zhou, L. Zheng, J. Wu, K. Li, Y. Ding, *ACS Energy Lett.* **2018**, *3*, 2150.
- [17] J. Zhang, J. Qian, J. Ran, P. Xi, L. Yang, D. Gao, *ACS Catal.* **2020**, *10*, 12376.
- [18] Z. Liu, Z. Xiao, G. Luo, R. Chen, C. L. Dong, X. Chen, J. Cen, H. Yang, Y. Wang, D. Su, Y. Li, S. Wang, *Small* **2019**, *15*, e1904903.
- [19] J. Suntivich, K. J. May, H. A. Gasteiger, J. B. Goodenough, Y. Shao-Horn, *Science* **2011**, *334*, 1383.
- [20] J. Lin, H. Wang, X. Zheng, Y. Du, C. Zhao, J. Qi, J. Cao, W. Fei, J. Feng, *J. Power Sources* **2018**, *401*, 329.
- [21] Y. Li, H. Zhang, M. Jiang, Q. Zhang, P. He, X. Sun, *Adv. Funct. Mater.* **2017**, *27*, 1702513.
- [22] L. Yu, J. Zhang, Y. Dang, J. He, Z. Tobin, P. Kerns, Y. Dou, Y. Jiang, Y. He, S. L. Suib, *ACS Catal.* **2019**, *9*, 6919.
- [23] Y. Chen, L. Su, M. Jiang, X. Fang, *J. Mater. Sci. Technol.* **2022**, *105*, 259.
- [24] D. Yan, Y. Li, J. Huo, R. Chen, L. Dai, S. Wang, *Adv. Mater.* **2017**, *29*, 1606459.
- [25] L. Zhuang, L. Ge, Y. Yang, M. Li, Y. Jia, X. Yao, Z. Zhu, *Adv. Mater.* **2017**, *29*, 1606793.
- [26] R. Liu, Y. Wang, D. Liu, Y. Zou, S. Wang, *Adv. Mater.* **2017**, *29*, 1701546.
- [27] L. Zheng, J. Song, X. Ye, Y. Wang, X. Shi, H. Zheng, *Nanoscale* **2020**, *12*, 13811.
- [28] L. Ma, S. Ma, H. Chen, X. Ai, X. Huang, *Appl. Surf. Sci.* **2011**, *257*, 10036.
- [29] M. Chauhan, K. P. Reddy, C. S. Gopinath, S. Deka, *ACS Catal.* **2017**, *7*, 5871.
- [30] L. Li, T. Tian, J. Jiang, L. Ai, *J. Power Sources* **2015**, *294*, 103.
- [31] J. Li, G. Liu, B. Liu, Z. Min, D. Qian, J. Jiang, J. Li, *Electrochim. Acta* **2018**, *265*, 577.
- [32] S. Lei, Q.-H. Li, Y. Kang, Z.-G. Gu, J. Zhang, *Appl. Catal. B* **2019**, *245*, 1.
- [33] M. Liu, Y. Fu, H. Ma, T. Wang, C. Guan, K. Hu, *Electrochim. Acta* **2016**, *191*, 916.
- [34] J. Bao, X. Zhang, B. Fan, J. Zhang, M. Zhou, W. Yang, X. Hu, H. Wang, B. Pan, Y. Xie, *Angew. Chem., Int. Ed.* **2015**, *54*, 7399.
- [35] L. Zhuang, Y. Jia, T. He, A. Du, X. Yan, L. Ge, Z. Zhu, X. Yao, *Nano Res.* **2018**, *11*, 3509.
- [36] L. Zhuang, Y. Jia, H. Liu, Z. Li, M. Li, L. Zhang, X. Wang, D. Yang, Z. Zhu, X. Yao, *Angew. Chem., Int. Ed.* **2020**, *59*, 14664.
- [37] Z. Liu, G. Wang, X. Zhu, Y. Wang, Y. Zou, S. Zang, S. Wang, *Angew. Chem., Int. Ed.* **2020**, *59*, 4736.
- [38] H. Jin, S. Mao, G. Zhan, F. Xu, X. Bao, Y. Wang, *J. Mater. Chem. A* **2017**, *5*, 1078.
- [39] M. S. Burke, M. G. Kast, L. Trotochaud, A. M. Smith, S. W. Boettcher, *J. Am. Chem. Soc.* **2015**, *137*, 3638.
- [40] W. Xiang, N. Yang, X. Li, J. Linnemann, U. Hagemann, O. Ruediger, M. Heidelmann, T. Falk, M. Aramini, S. DeBeer, M. Muhler, K. Tschulik, T. Li, *Nat. Commun.* **2022**, *13*, 179.
- [41] R. Li, Y. Guo, H. Chen, K. Wang, R. Tan, B. Long, Y. Tong, P. Tsiakaras, S. Song, Y. Wang, *ACS Sustainable Chem. Eng.* **2019**, *7*, 11901.
- [42] C. He, Z. Ma, Q. Wu, Y. Cai, Y. Huang, K. Liu, Y. Fan, H. Wang, Q. Li, J. Qi, Q. Li, X. Wu, *Electrochim. Acta* **2020**, *330*, 135119.
- [43] F. Li, J. Li, Q. Feng, J. Yan, Y. Tang, H. Wang, *J. Energy Chem.* **2018**, *27*, 419.
- [44] X. Yu, M. Zhang, W. Yuan, G. Shi, *J. Mater. Chem. A* **2015**, *3*, 6921.
- [45] S. Anantharaj, P. E. Karthik, S. Kundu, *Catal. Sci. Technol.* **2017**, *7*, 882.
- [46] S. Dresch, T. Ngo Thanh, M. Klingenhof, S. Brückner, P. Hauke, P. Strasser, *Energy Environ. Sci.* **2020**, *13*, 1725.
- [47] D. Friebel, M. W. Louie, M. Bajdich, K. E. Sanwald, Y. Cai, A. M. Wise, M.-J. Cheng, D. Sokaras, T.-C. Weng, R. Alonso-Mori, R. C. Davis, J. R. Bargar, J. K. Nørskov, A. Nilsson, A. T. Bell, *J. Am. Chem. Soc.* **2015**, *137*, 1305.
- [48] M. Gorlin, P. Chernev, J. Ferreira de Araujo, T. Reier, S. Dresch, B. Paul, R. Krahnert, H. Dau, P. Strasser, *J. Am. Chem. Soc.* **2016**, *138*, 5603.
- [49] S. Ye, Y. Lei, T. Xu, L. Zheng, Z. Chen, X. Yang, X. Ren, Y. Li, Q. Zhang, J. Liu, *Appl. Catal. B* **2022**, *304*, 120986.

- [50] P. Li, R. Chen, Y. Lin, W. Li, *Inorg. Chem. Front.* **2020**, *7*, 2611.
- [51] C. Qin, A. Fan, D. Ren, C. Luan, J. Yang, Y. Liu, X. Zhang, X. Dai, M. Wang, *Electrochim. Acta* **2019**, *323*, 134756.
- [52] L. Trotochaud, S. L. Young, J. K. Ranney, S. W. Boettcher, *J. Am. Chem. Soc.* **2014**, *136*, 6744.
- [53] A. Muthurasu, V. Maruthapandian, H. Y. Kim, *Appl Catal B* **2019**, *248*, 202.
- [54] H. Sun, W. Zhang, J.-G. Li, Z. Li, X. Ao, K.-H. Xue, K. K. Ostrikov, J. Tang, C. Wang, *Appl Catal B* **2021**, *284*, 119740.
- [55] A. A. Peterson, F. Abild-Pedersen, F. Studt, J. Rossmeisl, J. K. Nørskov, *Energy Environ. Sci.* **2010**, *3*, 1311.
- [56] J. J. Concepcion, R. A. Binstead, L. Alibabaei, T. J. Meyer, *Inorg. Chem.* **2013**, *52*, 10744.
- [57] C. C. L. McCrory, S. Jung, J. C. Peters, T. F. Jaramillo, *J. Am. Chem. Soc.* **2013**, *135*, 16977.
- [58] F. Song, X. Hu, *J. Am. Chem. Soc.* **2014**, *136*, 16481.
- [59] G. Kresse, J. Furthmüller, *Phys. Rev. B* **1996**, *54*, 11169.
- [60] G. Kresse, D. Joubert, *Phys. Rev. B* **1999**, *59*, 1758.
- [61] P. E. Blöchl, *Phys. Rev. B* **1994**, *50*, 17953.
- [62] J. P. Perdew, J. Chevary, S. H. Vosko, K. A. Jackson, M. R. Pederson, D. J. Singh, C. Fiolhais, *Phys. Rev. B* **1992**, *46*, 6671.
- [63] J. P. Perdew, Y. Wang, *Phys. Rev. B* **1992**, *45*, 13244.